PHYSICAL REVIEW B **79**, 205103 (2009)

Hybrid density functional theory applied to magnetite: Crystal structure, charge order, and phonons

Andrew D. Rowan and Charles H. Patterson
School of Physics, Trinity College Dublin, Dublin 2, Ireland

L. V. Gasparov
Department of Chemistry and Physics, University of North Florida, St. John's Bluff Road South, Jacksonville, Florida 32224, USA

(Received 18 November 2008; revised manuscript received 3 April 2009; published 5 May 2009)

The electronic structure and equilibrium structure of magnetite (Fe_3O_4) in the high temperature cubic $Fd\bar{3}m$ and low temperature monoclinic $P2/c$ unit cells have been computed using the Perdew-Wang generalized gradient approximation (GGA) to density functional theory (DFT) and the B3LYP hybrid density functional. The ground state for the GGA-DFT is an itinerant electron metallic state in the cubic unit cell and the ground state for the B3LYP functional is a charge ordered semiconducting state in the monoclinic unit cell. The equilibrium structure predicted by the B3LYP functional for Fe_3O_4 in the $P2/c$ unit cell has been calculated with lattice parameters fixed at values obtained in recent x-ray diffraction work and with the lattice fully relaxed. Bond lengths obtained with lattice parameters fixed at experimental values are in excellent agreement with x-ray measurements [J. P. Wright *et al.*, Phys. Rev. B **66**, 214422 (2002)]. The degree of charge order, measured as disproportionation of charge on octahedral B sites, is considerably less than unity and in reasonable agreement with values from resonant x-ray diffraction measurements. However, conduction electrons are found to be fully localized on B1 and B4 sites in orbitally ordered t_{2g} states. This shows that they are formally Fe^{2+} ions while Fe B2 and B3 sites are formally Fe^{3+} sites. Therefore Verwey's original conjecture regarding charge localization in Fe_3O_4 applies, even though the specific pattern of charge order is different. GGA-DFT and B3LYP density functionals were used to calculate phonons at the Γ point of the Brillouin zone. Phonon frequencies predicted for these crystal structures are compared to frequencies from infrared conductivity and Raman scattering experiments. Charge ordering causes symmetry breaking of force constants on symmetry lowering from the cubic $Fd\bar{3}m$ unit cell to the $P2/c$ unit cell. This produces frequency splitting of modes which are degenerate in the cubic unit cell and concentration of ion displacements in phonon eigenvectors on particular Fe octahedral B site chains, especially in the highest frequency bands.

DOI: 10.1103/PhysRevB.79.205103 PACS number(s): 78.30.−j, 71.15.Mb, 71.30.+h

I. INTRODUCTION

The crystal structure, charge, and orbital order of magnetite (Fe_3O_4) have been studied using a wide range of experimental[1–13] and theoretical[14–23] methods since the discovery of the Verwey transition in 1939.[1,2] Early refinements of the crystal structure of Fe_3O_4 below the Verwey transition temperature ($T_V \sim 120$ K) include neutron diffraction work by Iizumi and Shirane,[24] which used a detwinned crystal, and a single crystal x-ray study.[25] The neutron diffraction study showed the structure to have a monoclinic $\sqrt{2}a_c \times \sqrt{2}a_c \times 2a_c$ supercell with space group Cc,[24] where a_c [=8.3939 Å (Ref. 8)] is the lattice parameter of the high temperature cubic $Fd\bar{3}m$ phase. The most recent x-ray and neutron scattering data[8] provide a crystal structure for Fe_3O_4 below T_V which may be used to test the abilities of modern density functionals to predict properties of complex systems which undergo phase transitions.

In this paper we report calculations of the electronic structure, crystal structure, and Γ point phonons of Fe_3O_4 in the cubic and monoclinic unit cells using generalized gradient approximation (GGA)–density functional theory (DFT) or B3LYP hybrid DFT. Hybrid density functionals are so called because they contain a linear combination of density functional and Hartree-Fock (HF) approximations to the exchange potential. The B3LYP exchange-correlation potential is given in Eq. (1); it contains HF exchange with a weight $A=0.2$,

$$E_{xc} = (1-A)(E_x^{\text{LDA}} + BE_x^{\text{Becke}}) + AE_x^{\text{HF}} + (1-C)E_c^{\text{VWN}} + CE_c^{\text{LYP}}. \quad (1)$$

E_x^{LDA} (Ref. 26) is the local density approximation (LDA) to exchange; E_x^{Becke} is Becke's gradient corrected exchange functional;[27] E_c^{LYP} is the Lee-Yang-Parr approximation[28] to the correlation functional; E_c^{VWN} (Ref. 29) is the Vosko-Wilk-Nusair approximation[29] to the electron correlation functional. A, B, and C are weight parameters. Inclusion of HF exchange in a hybrid density functional may open a band gap in a calculation on an insulating oxide, for which DFT predicts no band gap; indeed, the band gap predicted by a hybrid density functional depends linearly and strongly on the weight of HF exchange used in the calculation, by about 0.1 eV % change in the value of A.[30] In the *GW* approximation[31,32] the HF exchange potential is screened by the inverse dielectric function and the corresponding "weight" of HF exchange depends on the wave vector and electron energy of a particular electron state. The effect of varying the parameter A about the value $A=0.2$ in the B3LYP functional, on band gap and charge order of Fe_3O_4, is investigated here.

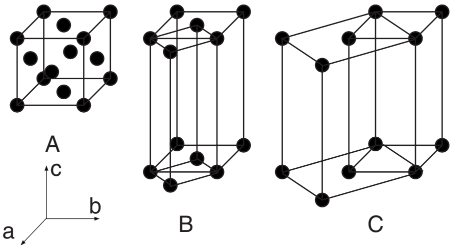

FIG. 1. (A) $Fd\bar{3}m$ unit cell, (B) $P2/c$ unit cell, and (C) Cc unit cell for Fe_3O_4. Solid spheres indicate common vertices of unit cells rather than atomic positions.

The recent refinement of the crystal structure of Fe_3O_4,[8,33] above and below T_V, employed both neutron and synchrotron x-ray powder-diffraction data at 130 and 90 K. It was found that a smaller $P2/c$ unit cell than the full Cc cell could account for almost all diffraction peaks.[8] The Cc unit cell contains 32 f.u. with 32 tetrahedral A sites and 64 octahedral B sites, of which 8 A and 16 B sites are unique. An NMR study[7] found spectral lines corresponding to all unique sites. Relationships between these unit cells are illustrated in Fig. 1. Figure 1(A) shows the cubic $Fd\bar{3}m$ cell. The $P2/c$ cell is derived from the $Fd\bar{3}m$ cell by doubling along the c axis and reducing cell vector lengths by $1/\sqrt{2}$ in the ab plane of the $Fd\bar{3}m$ cell [Fig. 1(B)]. The Cc cell is derived from the $P2/c$ cell by doubling in both a and b directions [Fig. 1(C)].

In the $Fd\bar{3}m$ Fe_3O_4 unit cell there are six Fe ions in two equivalent tetrahedral A sites and four equivalent octahedral B sites. All eight O ions are in equivalent sites. The primitive unit cell for the $P2/c$ phase (Fig. 1) contains eight Fe^{3+} ions with tetrahedral oxygen coordination in two crystallographic sites denoted A1 and A2, and $24Fe^{2+}$ and Fe^{3+} ions with octahedral coordination in six crystallographic sites denoted B1a, B1b, B2a, B2b, B3, and B4. The same notation is used here as was used by Wright *et al.* in Ref. 8. The arrangement of Fe ions in B sites consists of chains of B1 and B2 ions parallel to the a lattice translation vector, connected by O ions with 90° Fe-O-Fe bond angles. There are similar mixed chains of B3 and B4 ions parallel to the b vector. B1a and B1b and B2a and B2b ion pairs are almost crystallographically equivalent.[8] It is convenient to think of the $P2/c$ unit cell of Fe_3O_4 in terms of chains of corner sharing FeO_2 units, stacked in layers in the order B1, B3+B4, B2, B3+B4, connected by Fe A site ions, and alternating in direction from layer to layer (Fig. 2). There are eight O sites in the $P2/c$ cell of Fe_3O_4, labeled O1–O4, O5a, O5b, O6a, and O6b. Ions labeled a and b are in nearly equivalent sites. Where both a and b sites are referred to simultaneously in what follows, the a,b designation of sites is omitted.

The inverse spinel electronic structure of magnetite, $Fe^{3+}[Fe^{2+}Fe^{3+}]O_4^{8-}$, admits the possibility of ordering of charges on octahedral B sites as Fe^{2+} $3d^6$ and Fe^{3+} $3d^5$ ions in a symmetry broken state below T_V. Charge localization and ordering on B sites were originally proposed by Verwey and Haayman[2] to account for the 2 orders of magnitude reduction in electric conductivity when magnetite is cooled through T_V.[1,34] The Verwey model[35] is one in which Coulomb repulsions of ordered Fe^{2+} and Fe^{3+} on octahedral B sites are minimized. Coulomb repulsion minimization was reduced to a simple criterion by Anderson,[36] namely, that each Fe tetrahedron in the unit cell (formed, e.g., from two B1 ions in one chain and B3 and B4 ions in the chain beneath) should contain two Fe^{2+} and two Fe^{3+} ions. The pattern of charge order which has been found in first-principles calculations[15,18,19] is one where B1 and B4 sites are formally Fe^{2+} and B2 and B3 sites are formally Fe^{3+}; Anderson's criterion[36] is not met by this charge order pattern. Experimental data from recent resonant x-ray diffraction (RXD) studies[9,12,37] have been used to argue both for[9,12] and against[37] charge order in magnetite. RXD data were fitted to a model for charge ordering on Fe B sites which used charge disproportionation between Fe B1 and B2 sites (δ_{12}) and between B3 and B4 sites (δ_{34}). The values found for δ_{12} and δ_{34} were $0.12 \pm 0.025e$ and $0.10 \pm 0.06e$, respectively.[12] $\delta = 0.5e$ corresponds to complete disproportionation into Fe^{2+} and Fe^{3+} ions. Bond valence sums (BVSs) calculated for the structure determined by x-ray diffraction were used to argue that the degree of charge disproportionation predicted on the basis of B site Fe-O bond lengths[8] is very similar to that found by RXD.[9,12]

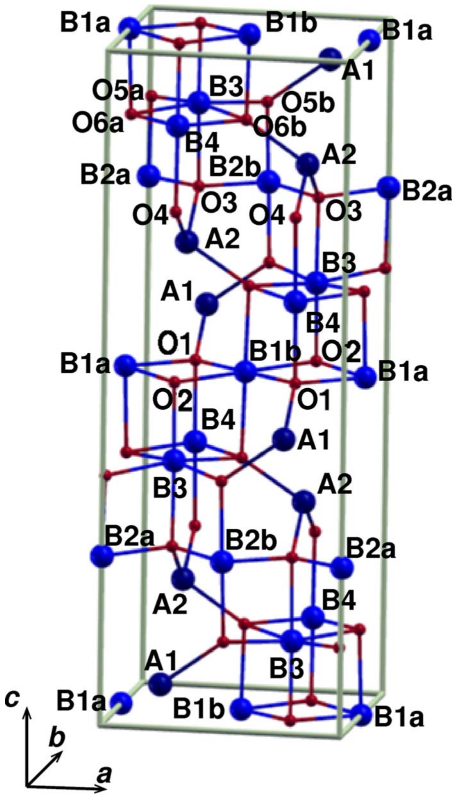

FIG. 2. (Color online) Primitive unit cell for Fe_3O_4 in the $P2/c$ unit cell. Octahedral Fe B site ions are shown as large light spheres, tetrahedral Fe A site ions are shown as large dark spheres, and O ions are shown as small spheres. B1 and B2 site ions form separate chains parallel to the a axis and B3 and B4 site ions form mixed chains parallel to the b axis.

Early measurements of the infrared (IR) vibrational spectrum of Fe_3O_4 were reported by Waldron in 1955.[38] White and DeAngelis[39] and Verble[40] assigned the Raman spectrum of Fe_3O_4 and many subsequent studies of both the IR (Refs.

41–43) and Raman spectra[41–45] have been reported. Several calculations of the phonon modes of the $Fd\bar{3}m$ cubic structure based on DFT have been reported recently.[21,22,46] Here we report calculations of Γ point phonon modes of both the cubic and monoclinic structures of Fe_3O_4 using either Perdew-Wang DFT-GGA (Ref. 47) or hybrid DFT functionals. The IR conductivity is calculated using a Lorentz oscillator (LO) model and compared to recent experimental data.[42] Densities of phonon modes of appropriate symmetry are compared to Raman spectra.[44] Phonon calculations for both structures were performed using the CRYSTAL electronic structure package[48] and employed the same basis set and similar computational conditions. It is therefore possible to make a direct comparison between the phonon modes predicted by the two calculations.

The unit cell of the monoclinic Cc phase of Fe_3O_4 below T_V contains 224 ions and contains too many ions for a phonon calculation using the CRYSTAL package on currently available computers. The unit cell of the $P2/c$ phase contains 56 ions; the phonon calculation for the smaller cell presented here is used to identify the character of the phonon modes which are observed in the low temperature phase of Fe_3O_4. A phonon calculation can also be used as a test of the stability of any equilibrium crystal structure since a saddle point on the potential energy surface manifests itself as an imaginary frequency of one or more phonon modes. Bond length distortions, which occur on going from the $Fd\bar{3}m$ to the $P2/c$ phase, break site symmetries of Fe and O ions. Phonon mode frequencies, which are degenerate in the $Fd\bar{3}m$ phase, split in the $P2/c$ phase and eigenvector amplitudes become concentrated on specific sites.

The equilibrium crystal structure of Fe_3O_4 found using both the GGA-DFT and B3LYP functionals is reported in Sec. II and compared to the structure found by x-ray diffraction.[8] The electronic structures of Fe_3O_4, obtained with either functional, are reported as well as charge and orbital order in the low temperature $P2/c$ unit cell. Results of calculations of phonons at the Γ point are presented for the $Fd\bar{3}m$ and $P2/c$ phases using the equilibrium crystal structures obtained using either the GGA-DFT or B3LYP functionals. In the discussion, the crystal structure of the $P2/c$ phase obtained from the B3LYP functional is compared with results of energy minimization DFT+U calculations. The charge order in the $P2/c$ phase is compared to that predicted by DFT+U or self-interaction corrected DFT (SIC-DFT) calculations; a brief discussion of application of hybrid density functional methods to transition metal oxides is given, followed by a discussion of the phonons and vibrational spectra of Fe_3O_4. Following the discussion and summary, details of calculations are given in the Appendix.

II. RESULTS

A. Crystal structure

Total energy minimization calculations were performed using GGA-DFT and B3LYP functionals. The high symmetry, high temperature $Fd\bar{3}m$ structure is a stable energy minimum on the potential energy surface when a GGA-DFT functional is used; when the B3LYP functional is used with the cubic cell and $Fd\bar{3}m$ space group symmetry constraints are relaxed, the energy minimized structure has no symmetry (space group P_1). When the B3LYP functional is used with the $P2/c$ cell the energy minimized structure closely resembles the structure obtained in recent x-ray diffraction experiments.[8]

Lattice parameters for the $P2/c$ unit cell from x-ray diffraction data at 90 K are $a=5.944\,407$, $b=5.924\,701$, $c=16.775\,15$ Å, and $\beta=90.2363°$ (Table II of Ref. 8). In this work the equilibrium structure of Fe_3O_4 in the $P2/c$ cell was calculated with the B3LYP functional, either by relaxing atomic positions with the lattice parameters fixed at these experimental values or by relaxing both atomic positions and lattice parameters simultaneously. These two structures are denoted below as “fixed” or “relaxed” according to whether atomic positions were relaxed with fixed or relaxed lattice parameters. Lattice parameters for the relaxed unit cell are $a=6.007\,88$, $b=6.014\,28$, $c=16.923\,49$ Å, and $\beta=90.000$. These lattice parameters exceed the experimental values by 1.1%, 1.5%, and 0.9%, respectively.

Fractional coordinates of ions in the $P2/c$ cell from the B3LYP functional calculation as well as coordinates from the work of Wright *et al.*[8] and Iizumi *et al.*[49] are given in Table I. Mean absolute differences in fractional coordinates and corresponding displacements of ion positions are also given in Table I for the fixed cell calculation.

In order to obtain a stable structure refinement, Wright *et al.*[8] imposed additional $Pmca$ pseudosymmetry constraints on Fe positions. Fe ions in B1a and B1b sites and in B2a and B2b sites were constrained to be equivalent.[8] Since these pseudosymmetry constraints are not imposed in our calculations, it is possible to see the extent of symmetry breaking which occurs about Fe B1 and B2 sites when these constraints are absent. Bond lengths derived from experimental and energy minimization data in Table I are given in Table II. When bond lengths are obtained from our computed atomic positions, the maximum difference in Fe B1 and B2 site Fe-O bond lengths is found to be 0.002 Å (Table II) showing that the assumption of equivalent sites is valid.

Bond lengths in all unique Fe B site octahedra from a B3LYP functional energy minimization calculation, with lattice parameters fixed at values from x-ray data, are shown in Fig. 3. The longest B site Fe-O bonds are B1 Fe-O2 and B1 Fe-O6, B4 Fe-O5 and B4 Fe-O6, and B4 Fe-O4 and B3 Fe-O3. The shortest B site Fe-O bonds are all bonds to Fe B2 and all bonds to Fe B3. When these are compared to bond lengths from x-ray data refinement[8] it is found that bonds to Fe B1 except bonds to O1 are long, all bonds to Fe B2 are short, bonds to Fe B3 except bonds to O5 are short, and bonds to Fe B4 except bonds to O1 are long. There is good overall agreement between bond lengths from experiment and the B3LYP functional calculation for both A and B site Fe-O bonds. Mean bond lengths from the B3LYP functional calculation, where lattice parameters were allowed to relax in the energy minimization calculation, are typically longer than those obtained with fixed lattice parameters by ~0.02 Å. Long/short alternation of Fe-O bond lengths in B site octahedra can be understood in terms of orientation of

TABLE I. Fractional atomic coordinates for Fe_3O_4 from experiment by Wright *et al.* (Ref. 8) and Iizumi *et al.* (Ref. 49) (italics) and total energy minimization. The total energy was minimized with the lattice parameters fixed at their experimental values and with the lattice parameters relaxed simultaneously with fractional atomic coordinates. Data by Wright *et al.* (Ref. 8) and Iizumi *et al.* (Ref. 49) were obtained using the $P2/c$ space group with $Pmca$ pseudosymmetry constraints. Data from this work were obtained using the $P2/c$ space group with no pseudosymmetry constraints. Lattice parameters are $a=5.944\,41$, $b=5.924\,72$, $c=16.775\,08$ Å, and $\beta=90.236°$ from experiment (Ref. 8) and $a=6.007\,88$, $b=6.014\,28$, $c=16.923\,49$ Å, and $\beta=90.000°$ when lattice parameters were fully relaxed. Mean absolute differences in fractional coordinates between experiment and the fixed unit cell calculation and the corresponding mean absolute displacements of ions are given at the bottom of the table.

	Expt.			Fixed			Relaxed		
Atom	x	y	z	x	y	z	x	y	z
A(1)	1/4	0.0034(4)	0.06366(7)	0.24922	0.00743	0.06406	0.25000	0.00800	0.06367
		0.0049(3)	*0.0635(1)*						
A(2)	1/4	0.5061(2)	0.18867(8)	0.25039	0.50335	0.18847	0.25000	0.50111	0.18873
		0.5067(2)	*0.1887(1)*						
B(1a)	0	1/2	0	0	1/2	0	0	1/2	0
B(1b)	1/2	1/2	0	1/2	1/2	0	1/2	1/2	0
B(2a)	0	0.0096(3)	1/4	0	0.00652	1/4	0	0.00422	1/4
		0.0099(3)							
B(2b)	1/2	0.0096(3)	1/4	1/2	0.00647	1/4	1/2	0.00421	1/4
		0.0099(3)							
B(3)	1/4	0.2659(2)	0.38010(9)	0.25032	0.26244	0.37940	0.25000	0.25997	0.37917
		0.2643(4)	*0.3789(1)*						
B(4)	1/4	0.7520(2)	0.37659(9)	0.25021	0.75225	0.37612	0.25000	0.75061	0.37608
		0.7549(5)	*0.3746(2)*						
O(1)	1/4	0.2637(7)	−0.0023(3)	0.25008	0.26275	−0.00222	0.25000	0.26313	−0.00210
		0.2630(6)	*−0.0027(2)*						
O(2)	1/4	0.7461(6)	−0.0029(3)	0.25007	0.75500	−0.00369	0.25000	0.75627	−0.00413
		0.7477(6)	*−0.0009(2)*						
O(3)	1/4	0.2447(8)	0.2542(3)	0.24989	0.23864	0.25400	0.25000	0.23566	0.25380
		0.2461(7)	*0.2450(2)*						
O(4)	1/4	0.7738(8)	0.2525(3)	0.24997	0.77398	0.25005	0.25000	0.77237	0.24972
		0.7696(6)	*0.2427(2)*						
O(5a)	−0.0091(4)	0.0095(6)	0.1277(2)	−0.00851	0.01345	0.13092	−0.00816	0.01224	0.13095
	−0.0116(6)	*0.0089(3)*	*0.1295(2)*						
O(5b)	0.4909(4)	0.0095(6)	0.3723(2)	0.49202	0.01361	0.36899	0.49185	0.01224	0.36905
	0.4884(6)	*0.0089(3)*	*0.3705(2)*						
O(6a)	−0.0081(4)	0.5046(6)	0.1246(2)	−0.00991	0.49338	0.12697	−0.01066	0.49071	0.12729
	−0.0067(6)	*0.5050(3)*	*0.1244(1)*						
O(6b)	0.4919(4)	0.5046(6)	0.3754(2)	0.49038	0.49367	0.37300	0.48934	0.49071	0.37271
	0.4933(6)	*0.5050(3)*	*0.3756(1)*						
Difference				0.0013	0.0046	0.0046			
Displacement				0.008	0.027	0.077			

ordered t_{2g} orbitals on B1 and B4 sites (see Sec. II C).

The crystal structure of Fe_3O_4 in the $Fd\bar{3}m$ cell is uniquely specified by one lattice parameter and one O ion coordinate parameter, x, which specifies the e Wyckoff position in the $Fd\bar{3}m$ space group. The experimental lattice parameters are 8.3963 Å and $x=0.254\,90$ (Ref. 8); the corresponding parameters derived from a B3LYP energy minimization calculation in which $Fd\bar{3}m$ symmetry constraints were applied to the atomic positions are 8.484 00 Å and $x=0.254\,25$. This is not the ground state for the 14 atom unit cell of the cubic phase of Fe_3O_4 using a B3LYP functional, instead the B3LYP functional predicts a charge or-

TABLE II. Fe-O bond lengths in Å for unique Fe ions derived from x-ray diffraction data and B3LYP functional energy minimization calculations for structures given in Table I. Mean bond lengths for each unique Fe ion site are given in angular brackets.

Bond	Expt.[a]	Fixed	Relaxed
A(1)-O(1)	1.898(4)	1.877	1.924
A(1)-O(5a)	1.875(2)	1.903	1.896
A(1)-O(5b)	1.882(2)	1.901	1.900
A(1)-O(2)	1.890(4)	1.879	1.924
⟨A(1)-O⟩	1.886(3)	1.890	1.911
A(2)-O(4)	1.913(5)	1.907	1.939
A(2)-O(6a)	1.870(2)	1.857	1.881
A(2)-O(6b)	1.877(2)	1.859	1.881
A(2)-O(3)	1.899(5)	1.915	1.931
⟨A(2)-O⟩	1.890(4)	1.885	1.908
B(1a)-O(1) × 2	2.042(3)	2.046	2.070
B(1a)-O(6a) × 2	2.091(3)	2.131	2.156
B(1a)-O(2) × 2	2.082(3)	2.121	2.153
⟨B(1)-O⟩	2.072(3)	2.099	2.126
B(1b)-O(1) × 2	2.042(3)	2.045	2.070
B(1b)-O(6b) × 2	2.091(3)	2.131	2.156
B(1b)-O(2) × 2	2.082(3)	2.120	2.153
⟨B(1)-O⟩	2.072(3)	2.099	2.126
B(2a)-O(5a) × 2	2.052(3)	1.998	2.049
B(2a)-O(4) × 2	2.040(3)	2.026	2.049
B(2a)-O(3) × 2	2.038(4)	2.025	2.016
⟨B(2)-O⟩	2.043(3)	2.016	2.038
B(2b)-O(5b) × 2	2.052(3)	1.997	2.049
B(2b)-O(4) × 2	2.040(3)	2.026	2.049
B(2b)-O(3) × 2	2.038(4)	2.027	2.016
⟨B(2)-O⟩	2.043(3)	2.016	2.038
B(3)-O(5a)	2.092(3)	2.066	2.088
B(3)-O(5b)	2.092(3)	2.066	2.088
B(3)-O(6a)	2.018(3)	1.981	2.001
B(3)-O(6b)	2.018(3)	1.981	2.001
B(3)-O(2)	1.964(5)	1.964	1.977
B(3)-O(3)	2.116(5)	2.108	2.127
⟨B(3)-O⟩	2.050(4)	2.027	2.047
B(4)-O(5a)	2.094(3)	2.115	2.145
B(4)-O(5b)	2.094(3)	2.117	2.145
B(4)-O(6a)	2.053(3)	2.096	2.125
B(4)-O(6b)	2.053(3)	2.095	2.125
B(4)-O(1)	2.033(5)	2.043	2.063
B(4)-O(4)	2.086(5)	2.119	2.145
⟨B(4)-O⟩	2.069(4)	2.098	2.125

[a] Reference 8.

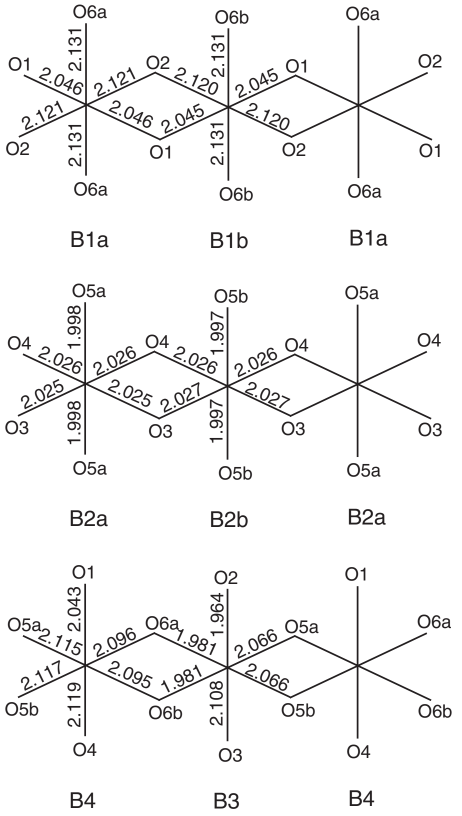

FIG. 3. Fe-O bond lengths around octahedral Fe sites from a B3LYP functional energy minimization calculation with lattice parameters fixed at values determined by x-ray diffraction (Table I, fixed column).

dered semiconducting state which breaks $Fd\bar{3}m$ symmetry when symmetry constraints are relaxed. The cubic phase of Fe_3O_4 was also studied using a DFT-GGA functional; in this case the ground state is an itinerant electron metallic state with $Fd\bar{3}m$ symmetry and equilibrium lattice constants, $a_c = 8.3777$ Å and $x = 0.254\,99$.

B. Electronic structure

The $Fd\bar{3}m$ space group and lattice for Fe_3O_4 above T_V are the same as for the diamond structure, so they share the same familiar Brillouin zone. The band structure and density of states obtained using the DFT-GGA functional in the $Fd\bar{3}m$ unit cell are shown in Figs. 4 and 5; no shift of energy eigenvalues has been applied to energy bands. The majority spin band gap is 3.6 eV and the minority spin band structure has four bands occupied by two electrons close to the Fermi level at −1.2 eV.

The majority spin band structure for Fe_3O_4 in the $P2/c$ unit cell (Fig. 6) has a band gap of 3.2 eV. The minority spin band structure has eight narrow filled bands around −2 eV, which contain the valence band maximum. The band structure shown uses high symmetry points of the Brillouin zone for which wave vectors are parallel to the *ab* plane of the crystal. There is little dispersion for wave vectors parallel to the long *c* axis, as expected. The band gap is 0.87 eV and the gap separates occupied states on Fe B1 and B4 sites from unoccupied states on B2 and B3 sites. Figure 7 shows the density of states projected onto B sites. Occupied majority spin Fe states are nearly exclusively B site states while oc-

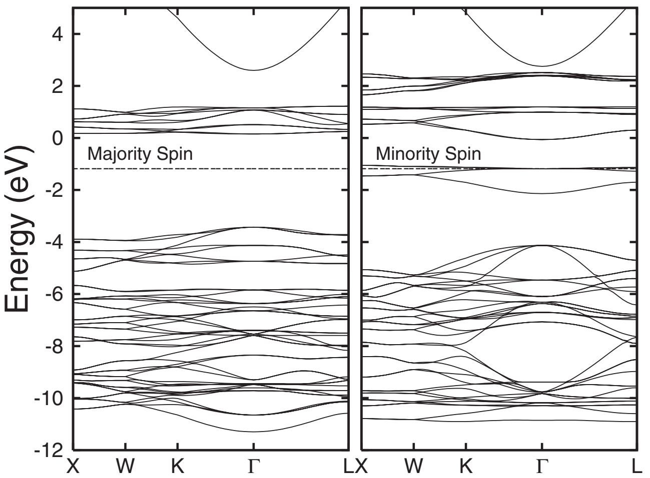

FIG. 4. Electronic band structure of magnetite in the $Fd\bar{3}m$ unit cell. The Fermi energy is shown as a dashed line.

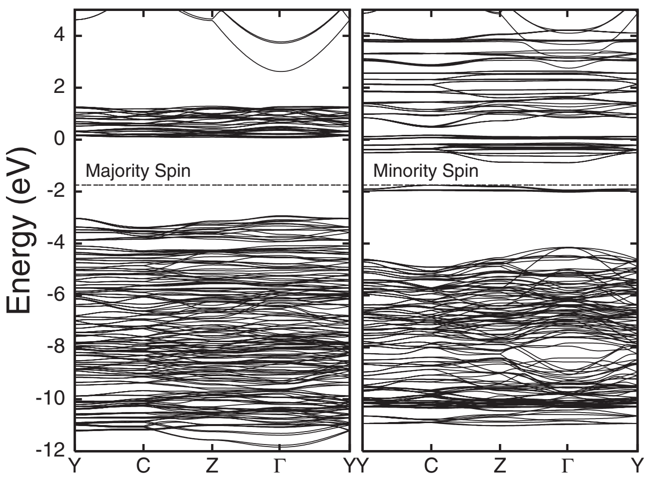

FIG. 6. Electronic band structure of Fe_3O_4 in the $P2/c$ unit cell. The valence band maximum is shown as a dashed line.

cupied minority spin Fe states (not shown) are nearly exclusively A site states, as expected for an inverse spinel ferrimagnetic state.

C. Charge and orbital order

The original model for charge order in magnetite[2,35,50] set forward by Verwey had chains of octahedral Fe ions which were either Fe^{2+} or Fe^{3+}. These chains are the B1, B2, and mixed B3/B4 chains illustrated in Fig. 2. The structure of magnetite can be viewed as a lattice of corner sharing Fe_4O_4 cubes formed by perpendicular chains in adjacent vertical layers. The four Fe ions in each cube are arranged in a tetrahedron and there are two types of cube, containing B1a-B1b-B3-B4 and B2a-B2b-B3-B4 ions. On the grounds that electrostatic repulsions of ordered charges dominate the total energy in magnetite, Anderson[36] argued that there should be two Fe^{2+} and two Fe^{3+} ions in each type of cube. Fe tetrahedra formed by intersecting chains in the Verwey model therefore had two ions of each valence and fulfilled the Anderson criterion[3] for minimal Coulomb repulsion.

These ideas have been contradicted recently by several DFT+U calculations[15,16,19] and conclusions of experimental

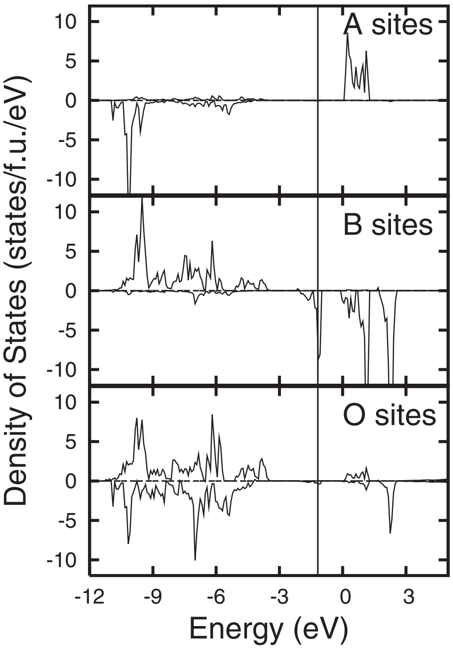

FIG. 5. Density of states for Fe_3O_4 in the $Fd\bar{3}m$ unit cell from a DFT-GGA calculation projected onto tetrahedral and octahedral Fe and O sites. The Fermi energy is marked by a vertical line at −1.2 eV.

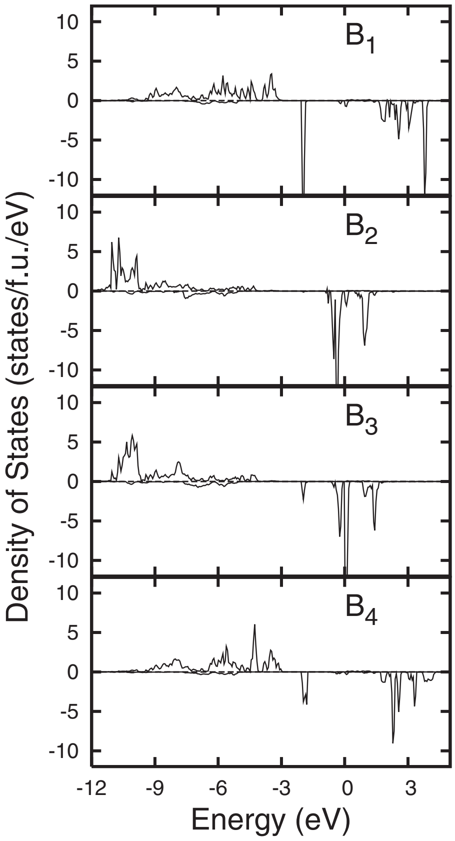

FIG. 7. Density of states for Fe_3O_4 in the $P2/c$ unit cell projected onto Fe B sites.

TABLE III. Magnetite Mulliken net charge populations and magnetic moments on Fe A and B sites.

Site	Net charge e	Magnetic moment μ_B
A1	2.10	−4.15
A2	2.10	−4.15
B1	1.83	3.76
B2	2.17	4.26
B3	2.11	4.18
B4	1.81	3.73

work.[8] Mulliken net charge populations and magnetic moments for magnetite with equilibrium atomic positions obtained with lattice parameters fixed at experimental values are given in Table III. Fe $3d$ orbital populations from B3LYP functional calculations are compared to populations derived from several DFT+U and a SIC-DFT calculation in Table IV.

Net charges on B site Fe ions range between 1.81e and 2.17e. B1 and B4 sites have charges of 1.81e and 1.83e, respectively, and B2 and B3 sites have charges of 2.17e and 2.11e, respectively. Differences in net charges of B1a and B1b and B2a and B2b ions are less than 0.001e. Magnetic moments of B1 and B4 sites are 3.76μ_B and 3.73μ_B and moments of B2 and B3 sites are 4.26μ_B and 4.17μ_B. The charge disproportionation parameters δ_{12} and δ_{34} introduced in Sec. I are 0.18 and 0.16 between B1/B2 and B3/B4 sites, somewhat larger than those derived from RXD, 0.12 and 0.10, respectively.[12] When the HF exchange weight parameter in Eq. (1) is reduced to 0.15, these values change to 0.14 and 0.08 and straddle the experimentally derived values. Table IV shows that charge and spin disproportionation is explained by Fe $3d$ orbital populations. B1 and B4 sites have $3d$ populations of 6.10e and 6.13e, close to the formal value of 6e for an Fe^{2+} ion. B2 and B3 sites have $3d$ populations of 5.66e and 5.71e, closer to formal populations of Fe^{2+} than Fe^{3+}. Inspection of Table IV also shows that Fe $3d$ populations predicted by the B3LYP functional lie within the range of $3d$ populations obtained in three DFT+U calculations[15,17,20] and that $3d$ populations predicted by a SIC-DFT calculation[14] lie well outside this range. Band gaps predicted by DFT+U calculations range from 0.0 to 0.2 eV, the SIC-DFT band gap is 0.35 eV, and the B3LYP band gap is 0.87 eV. As noted earlier, the band gap predicted in hybrid functional calculations depends sensitively on the weight of HF exchange used. When the HF exchange weight parameter is reduced to $A=0.15$, the predicted band gap is reduced to 0.32 eV. Differences in single particle energy eigenvalues in DFT calculations cannot be interpreted as ionization potentials, strictly speaking. Disappearance of the gap, however, does indicate the onset of metallic behavior.

TABLE IV. Comparison of Fe_3O_4 Mulliken charge populations on octahedral and tetrahedral Fe $3d$ sites and band gaps in eV predicted by B3LYP, DFT+U, and SIC-DFT methods.

Site	B3LYP	DFT+U [a]	DFT+U [b]	DFT+U [c]	SIC-DFT[d]
A1	5.73			5.70	6.56
A2	5.73			5.70	6.56
B1	6.10	5.57	6.04	5.95	7.74
B2	5.66	5.41	5.73	5.66	7.45
B3	5.71	5.44	5.92	5.72	7.15
B4	6.13	5.58	6.03	5.92	7.35
Band gap	0.87	0.2	0.14	0.0	0.35

[a] Reference 15.
[b] Reference 20.
[c] Reference 17.
[d] Reference 14.

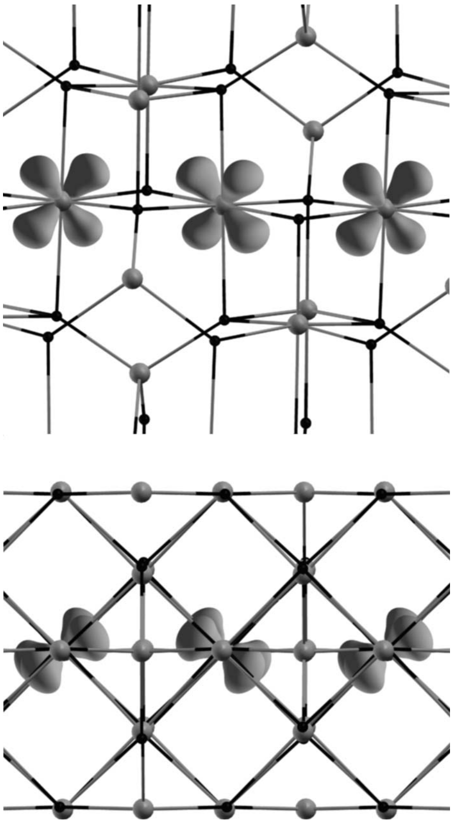

FIG. 8. Charge density difference plot for Fe B1 sites of Fe_3O_4. (Top panel) View along b crystallographic axis; (bottom panel) view along c axis.

Charge order in magnetite is visualized in charge density difference plots in Figs. 8 and 9. Charge density difference plots are generated by subtracting a superposition of self-consistent densities of Fe^{3+} and O^{2-} ions in vacuum from the self-consistent density for the Fe_3O_4 crystal. The difference function shows the distribution of the eight electrons per unit cell omitted from the reference density.

Figure 8 shows the charge density difference in the vicinities of the B1a and B1b sites. The charge ordered electron is in a t_{2g} state and lies roughly within the four O2 and O6 ions illustrated in Fig. 3 (top panel). The presence of this orbital ordered electron explains the long B1 Fe-O2 and Fe-O6 bonds. A similar plot for the B2 site (not shown) shows no indication of extra charge on that site. Figure 9 shows a charge density difference plot for the plane containing the B3 and B4 sites. The B3 site shows only a diffuse spherical

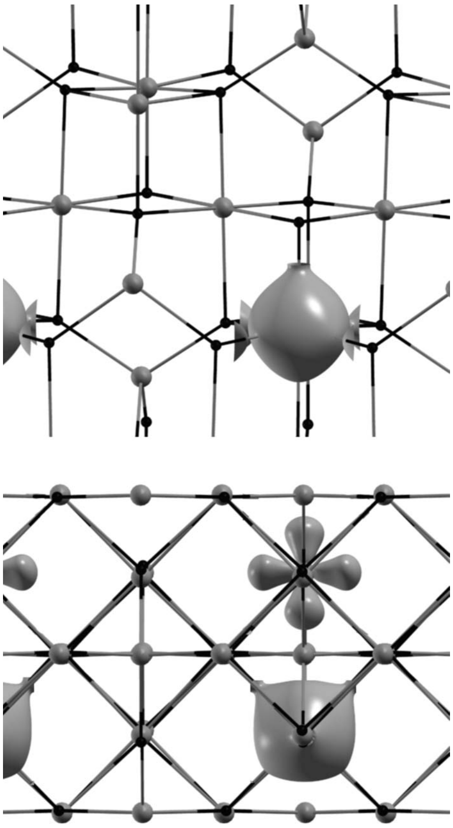

FIG. 9. Charge density difference plot for Fe B3 and B4 sites of Fe_3O_4. (Top panel) B3 sites viewed along crystallographic *a* axis; (bottom panel) B3 and B4 sites viewed along *c* axis.

isosurface and no charge localization, while the B4 site shows an electron in a t_{2g} orbital lying in the *ab* plane of the $P2/c$ unit cell. The orbital ordered electron on the B4 site explains the long B4 Fe-O5 and Fe-O6 bonds (Fig. 3, bottom panel).

Patterns of bond lengths around the B1 site from x-ray data[8] and the B3LYP calculation are the same: bonds ranging in length from 2.120 to 2.131 Å are predicted by the B3LYP calculation in the plane around B1 sites containing the t_{2g} electron. There are shorter bonds ranging from 2.045 to 2.046 Å in the direction perpendicular to that plane. The ordered orbital on B4 sites lies parallel to the *ab* crystallographic plane. Fe-O bonds at B4 sites range between 2.095 and 2.117 Å while there is one long Fe-O bond (2.119 Å) and one short bond (2.043 Å) perpendicular to the plane containing the orbital order. Bond lengths around B2 sites are nearly equivalent, ranging from 1.997 to 2.026 Å in length. Bond lengths around B3 sites range from 1.981 to 2.108 Å even though there is apparently no orbital order on that site (Fig. 9). A similar pattern of charge order has been found in DFT+U calculations.[15,16,19]

D. Lorentz oscillator model for IR conductivity

In order to compare results of phonon calculations to phonons observed as peaks in IR conductivity measurements,[42] the IR conductivity was calculated using a LO model. The conductivity tensor $\sigma(\omega)$ is given by a sum over phonon modes,

$$\sigma(\omega/\text{cm}^{-1}) = \frac{\omega}{60\epsilon_o V}\sum_i \frac{Z_i Z_i^T \gamma\omega}{(\omega_i^2-\omega^2)^2+(\gamma\omega)^2}, \qquad (2)$$

$$Z_i = \frac{z_j x_{ij}}{\sqrt{m_j}}, \qquad (3)$$

where ω_i are phonon frequencies, γ is a damping parameter, chosen to be 6 cm^{-1}, z_j are Born charges, x_{ij} is the jth component of the ith phonon eigenvector, m_j are atomic masses, and V is the unit cell volume. It was not possible to obtain Born charges for Fe_3O_4 using the CRYSTAL package, so instead Born charges of $+2.67e$ and $-2.00e$ were used for all Fe and O ions, respectively.

TABLE V. Phonon frequencies in $Fd\bar{3}m$ magnetite from experiment and DFT-GGA calculations in cm^{-1}.

DFT[a]	DFT[b]	DFT[c]	Expt.[d]	Irrep.	Activity
147	136	148		T_{2u}	
196	161	188	200	T_{1u}	IR
204	170			E_u	
208	195	235	193	T_{2g}	R
334	267			T_{1g}	
343	309			T_{1u}	IR
353	287	293		A_{2u}	
363	265		308	E_g	R
389	323	327	350	T_{1u}	IR
410	344			T_{2u}	
465	400		450	T_{2g}	R
522	423			E_u	
562	538		560	T_{1u}	IR
565	525		540	T_{2g}	R
584	589		670	A_g	R
657	598			A_{2u}	

[a] This work.
[b] Reference 22.
[c] Reference 46.
[d] Reference 42.

E. Phonons in the high temperature *Fd*$\bar{3}$*m* unit cell

Symmetry analysis of the $Fd\bar{3}m$ structure of magnetite shows that the 42 vibrational+translational modes consist of 12 Raman active modes ($A_g+E_g+3T_{2g}$), 15 IR active modes ($5T_{2u}$), 3 of which are translational modes, and 15 optically inactive modes ($2B_u+2E_u+T_{1g}+2T_{2u}$). Mode frequencies from experiment, the present work, and other DFT-GGA calculations are shown in Table V. Basis sets, k point sampling conditions, etc., used in calculations reported in this work are described in the Appendix.

IR active modes are found in experiment at room temperature at 200, 350, and 560 cm^{-1}; the mode around

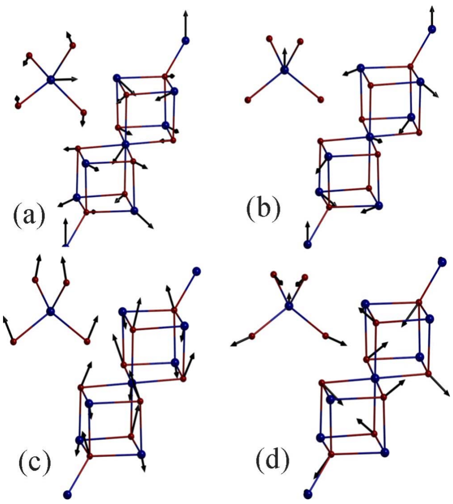

FIG. 10. (Color online) IR active phonon mode eigenvectors of T_{1u} symmetry from DFT-GGA calculation on Fe_3O_4 in the $Fd\bar{3}m$ unit cell. Mode frequencies are (a) 196 cm^{-1}, (b) 343 cm^{-1}, (c) 389 cm^{-1}, and (d) 562 cm^{-1}. Displacements of O ions about tetrahedrally coordinated Fe^{3+} A site ions are shown separately for each mode.

200 cm^{-1} is weak in the most recent data[42] and is completely absent from the earlier data of Degiorgi *et al.*[41] The modes at 350 and 560 cm^{-1} are the main features in the vibrational IR conductivity spectrum at room temperature. The three DFT-GGA calculations in Table V predict the lowest T_{1u} mode frequency between 161 and 196 cm^{-1}. Higher T_{1u} modes are predicted to lie between 309 and 343 cm^{-1}, between 323 and 389 cm^{-1}, and between 538 and 562 cm^{-1}. The two highest frequency T_{1u} modes carry the great majority of the IR oscillator strength in an LO model of the IR conductivity. Frequencies for these two modes are predicted to be 389 and 562 cm^{-1} in this work; these compare well with experimental values of 350 and 560 cm^{-1}.[42] The IR spectrum at room temperature therefore consists of the following: a T_{1u} mode at 200 cm^{-1} with little oscillator strength; a second T_{1u} mode, predicted to lie at 343 cm^{-1}, is a weak shoulder in the strongest mode, which is observed at 350 cm^{-1} and predicted at 389 cm^{-1}; and the highest T_{1u} mode is at 560 cm^{-1}, in good agreement with the predicted value of 562 cm^{-1}. Ion displacements in IR active phonons in $Fd\bar{3}m$ Fe_3O_4 are illustrated in Fig. 10.

Raman active modes are observed in experiment at room temperature at 193, 308, 540, and 670 cm^{-1} by Gasparov *et al.*[42] and at 193, 306, 538, and 668 cm^{-1} by Shebanova and Lazor.[44] There is therefore good agreement between these recent studies. Shebanova and Lazor[44] assigned the modes at 193 and 538 cm^{-1} to T_{2g} modes and the modes at 306 and 668 cm^{-1} to E_g and A_g modes, respectively. They assigned a weak feature observed at 490 cm^{-1} in another study[51] to the third T_{2g} mode. There is a weak peak at 450 cm^{-1} in the room temperature data in Ref. 42. The ranges of positions of Raman active modes predicted by the DFT calculations in Table V are 195–235, 400–465, and 525–565 cm^{-1} for T_{2g} modes, 265–363 cm^{-1} for the E_g mode, and 584–589 cm^{-1} for the A_g mode. Eigenvectors for Raman active modes in $Fd\bar{3}m$ Fe_3O_4 from the GGA-DFT calculation are shown in Fig. 11. The assignment by Shebanova and Lazor[44] is therefore in agreement with the mode frequencies from these DFT calculations.

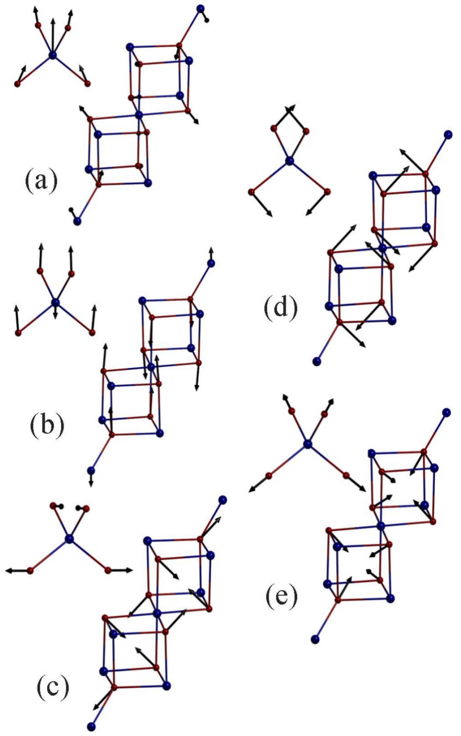

FIG. 11. (Color online) Raman active phonon mode eigenvectors from DFT-GGA calculations on Fe_3O_4 in the $Fd\bar{3}m$ unit cell. Mode frequencies and symmetries are (a) 223 cm^{-1} T_{2g}, (b) 465 cm^{-1} T_{2g}, (c) 565 cm^{-1} T_{2g}, (d) 363 cm^{-1} E_g, and (e) 584 cm^{-1} A_g. Displacements of O ions about tetrahedrally coordinated Fe^{3+} A site ions are shown separately for each mode.

F. Phonons in the low temperature $P2/c$ unit cell

There are 56 ions in the $P2/c$ unit cell of Fe_3O_4; the 168 vibrational+translational modes at the Γ point of the Brillouin zone consist of $38A_g+40B_g+44A_u+46B_u$ modes. Symmetry operations for the $P2/c$ space group with a unique b axis are E, $C_2(y)+0.5z$, i, and $\sigma_h+0.5z$. A (B) modes are even (odd) with respect to the C_2 rotation, g (u) modes are even (odd) with respect to inversion, the A_g and B_u modes are even with respect to the mirror plane, and the A_u and B_g modes are odd. Figure 2 shows that B1a Fe ions lie on the C_2 axis and B2 Fe ions almost lie in the mirror plane. A_u and B_u modes are IR active and couple to electric fields polarized along the y and x,z axes, respectively, when the unique axis is b and x, y, and z axes are parallel or almost parallel to the a, b, and c axes. A_g and B_g modes are Raman active. A_g modes are detected in an XX experimental geometry[44] in which incident and scattered radiations have the same polarization, while B_g modes are detected in an XY geometry where polarizations of incident and scattered radiations are at right angles.

Experimental IR conductivity data for Fe_3O_4 at 40 K from Ref. 42 are reproduced in Fig. 12 and show two strong bands

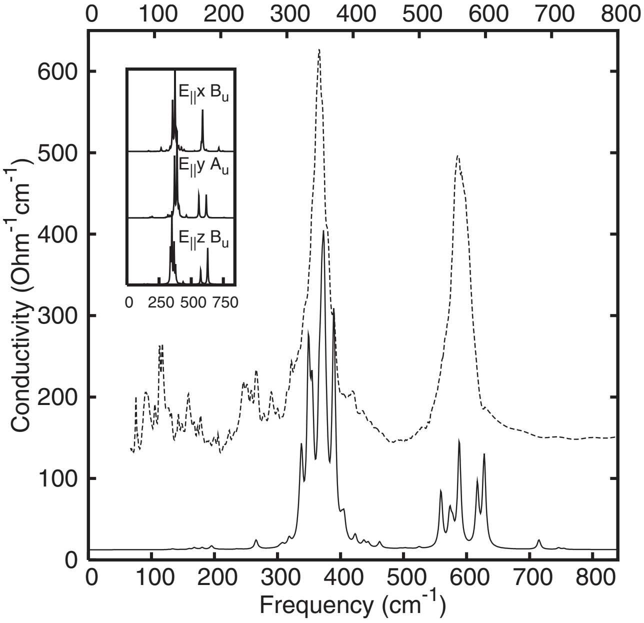

FIG. 12. IR conductivity of Fe_3O_4 at 40 K reproduced from Ref. 42 (dotted curve) and from an LO model using phonon modes from B3LYP calculation on Fe_3O_4 in the $P2/c$ unit cell (solid curve). The orientationally averaged spectrum from the LO model is drawn with a scale which differs from that for experiment by 5%, as explained in the text. Inset shows the decomposition of the averaged IR conductivity into components excited by electric field vectors aligned with Cartesian x, y, and z axes.

between 300 and 400 cm^{-1} and between 550 and 650 cm^{-1}. There are also bands around 100 and 250 cm^{-1}. The LO model in Eq. (2) was used to calculate the conductivity of Fe_3O_4 using A_u and B_u phonon eigenmodes. Vibrational frequencies (and other properties such as band gap[30]) predicted by hybrid DFT methods depend quite sensitively on the weight of HF exchange used in calculations; in the case of Fe_3O_4, increasing the weight from 20% (B3LYP) to 30% increases mode frequencies in Fe_3O_4 by 10%. When the experimental data and the results of the LO model are compared, it is clear that peaks in the IR conductivity from the LO model are too high in frequency by about 5%. The results of the LO model and the experimental data are plotted in Fig. 12 with scales that differ by 5% so that the scaled LO model curve can be directly compared to experiment. The main LO model curve in Fig. 12 shows orientationally averaged conductivities for electric fields applied along three Cartesian directions. The inset of Fig. 12 shows LO model conductivities for each applied field direction. Inspection of the inset shows that the modes in the higher frequency IR band occur as split pairs for fields along the x and y (a and b crystallographic) directions. This splitting arises because of charge order on octahedral B sites.

The IR active T_{1u} mode predicted by DFT-GGA at 389 cm^{-1} in the $Fd\bar{3}m$ unit cell and observed in experiment around 350 cm^{-1} (Table V) is replaced by $10A_u$ and $12B_u$ modes in the range of 300–400 cm^{-1} in the B3LYP calculation. The mode predicted by DFT-GGA at 562 cm^{-1} in the $Fd\bar{3}m$ unit cell and observed in experiment around 560 cm^{-1} (Table VI) is replaced by $5A_u$ and $5B_u$ modes in the range of 550–650 cm^{-1} in the B3LYP calculation. Mode frequencies and concentration of eigenvector amplitudes on specific sites in the $P2/c$ unit cell, for the four most optically active A_u and B_u modes in each band, are given in Table VI. Modes with greatest IR activity in the band between 300 and 400 cm^{-1} are found at 370 and 389 cm^{-1} (A_u) and at 349 and 373 cm^{-1} (B_u). Modes with greatest IR activity in the band between 550 and 650 cm^{-1} are found at 559 and 617 cm^{-1} (A_u) and at 573 and 627 cm^{-1} (B_u) (Fig. 12). Ion displacements in IR active phonons with the largest optical activity in the band between 300 and 400 cm^{-1} are available in Ref. 52.

TABLE VI. Strongly IR active phonon modes in $P2/c$ magnetite from B3LYP calculations. Ion sites on which phonon eigenvector amplitudes are primarily concentrated and mode frequencies in cm^{-1} are given.

Freq.	Irrep.	Eigenvector
370	A_u	B4 O4 O5 O6
389	A_u	B2 B3 O1 O3 O5 O6
349	B_u	B2 O4
373	B_u	B2 B3 O1 O4 O5 O6
559	A_u	O3 O4
617	A_u	O1 O2
573	B_u	O5
627	B_u	B2 O6

Inspection of the A_u mode eigenvectors at 370 and 389 cm^{-1} shows that ion displacements in these modes are concentrated on specific B site chains. The mode at 370 cm^{-1} is concentrated on B4, O5, and O6 sites of the B3/B4 chain and especially on O4 sites in the B2 chain (Table VI). The mode at 389 cm^{-1} is concentrated on B3, O5, and O6 sites in the B3/B4 chain and also on the B2 and O3 sites in the B2 chain. These modes are similar in character but are concentrated either on O3 or O4 ions in the B2 chain. The 349 cm^{-1} B_u mode eigenvector is strongly concentrated on B2 and O4 sites in the B2 chains and the 374 cm^{-1} mode eigenvector is spread over all B site layers. Charge order must induce changes in force constants for interactions between Fe ions and their O neighbors. Symmetry breaking in magnitudes of force constants on going from the cubic $Fd\bar{3}m$ unit cell to the $P2/c$ monoclinic cell will result in ion displacements in specific modes becoming concentrated on specific ions and splitting of frequencies of phonons which are degenerate in the cubic unit cell. The extent of concentration of modes on specific O ions is much greater for the higher frequency IR and Raman active bands which predominantly involve O ion displacements.

The IR conductivity band between 550 and 650 cm^{-1} is generated by modes which are essentially completely concentrated on O ions. They consist of out-of-phase A site Fe-O stretching in both the $Fd\bar{3}m$ and $P2/c$ unit cells. In the $P2/c$ unit cell, modes are concentrated on O ions in particular B site chains, whereas in the $Fd\bar{3}m$ unit cell, symmetry dictates that displacement amplitudes on each O ion are equal in magnitude. The 559 cm^{-1} A_u mode in Fig. 13(a) is concentrated on O3 and O4 ions in B2 chains, the 617 cm^{-1} A_u mode is concentrated on O1 and O2 ions in B1 chains, the 573 cm^{-1} B_u mode is concentrated on O5 ions, and the 627 cm^{-1} B_u mode is concentrated on B2 and O6 ions.

The pattern of concentration of ion displacements on specific sites can be explained by charge order on B sites. The charge order described in Sec. II C shows that Fe ions in B2 chains are formally Fe^{3+} while Fe ions in B1 chains are formally Fe^{2+}. B_u modes in Figs. 13(c) and 13(d) are concentrated on B3/B4 chains but are split between O5 and O6 sites. O5 ions are bonded to B2 sites (Fe^{3+}) in the chain above or below, while O6 ions are bonded to B1 sites (Fe^{2+}) above or below. This difference in environment is sufficient to split the mode frequencies by 54 cm^{-1}. Obviously, the greater the extent of charge ordering, the larger the splitting will be.

Since single modes in the $Fd\bar{3}m$ phase are replaced by multiple modes in the $P2/c$ phase, broadening of IR band linewidths in experiment might be expected on cooling through T_V. Linewidths and frequency shifts in IR and Raman active modes which accompany the Verwey transition were reported previously.[42] The 300–400 cm^{-1} band linewidth increases from 24 to 39 cm^{-1} and the 550–650 cm^{-1} band linewidth increases from 26 to 36 cm^{-1} on cooling through T_V. The experimental linewidth is too broad to distinguish individual modes in the $P2/c$ phase, but the 300–400 cm^{-1} band is certainly more asymmetric below T_V. However, the linewidth of the strong Raman line around 670 cm^{-1} actually decreases from 30 to 20 cm^{-1} on cooling through T_V.[42]

The Raman spectrum for $\mathrm{Fe_3O_4}$ at 5 K is shown in Fig. 14 for both XX and XY experimental geometries. Changes in the Raman spectrum in the XX experimental geometry on warming to 300 K are shown in the inset of Fig. 14. There are dramatic changes in the Raman spectrum in the XX experimental geometry on cooling below T_V, in particular a mode appears around 165 cm^{-1}, a broad band of modes appears between 200 and 500 cm^{-1}, and a shoulder to the A_g mode at 670 cm^{-1} appears around 650 cm^{-1}. It is not possible to calculate Raman cross sections using the CRYSTAL package. Instead the A_g and B_g densities of modes at the Γ point are compared to experimental spectra by representing each mode as a Lorentzian with a full width at half maximum (FWHM) of 6 cm^{-1}. Frequency axis scales which differ by 5% for B3LYP calculation and experimental mode frequencies are used in the same manner as for the IR spectrum in Fig. 12. There are less dramatic changes in the XY geometry experimental spectrum (Fig. 14) on cooling through T_V. There is reasonable agreement between the density of modes from the B3LYP calculation and the positions of experimental lines in the XX and XY geometries, except below 250 cm^{-1} in the XY geometry.

The most intense Raman lines in the room temperature spectrum of $\mathrm{Fe_3O_4}$ are the T_{2g} and A_g modes predicted by the DFT-GGA calculation in this work to lie at 565 and 584 cm^{-1}, respectively. Experimental lines are observed at 540 and 670 cm^{-1}. The B3LYP calculation on $\mathrm{Fe_3O_4}$ in the $P2/c$ unit cell predicts $4A_g$ and $4B_g$ modes between 560 and 640 cm^{-1} and $4A_g$ and $4B_g$ modes between 650 and 800 cm^{-1}. These groups of modes replace the highest frequency T_{2g} and A_g modes observed above T_V.

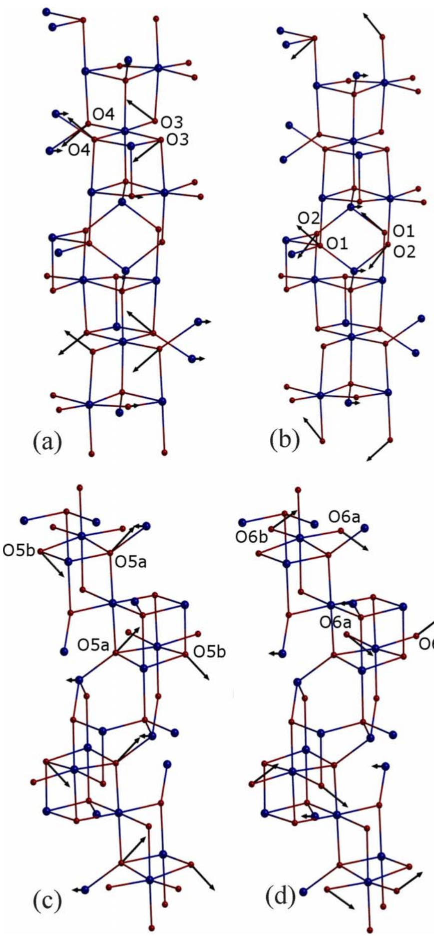

FIG. 13. (Color online) Phonon eigenvectors with largest optical activity in the band between 550 and 650 cm^{-1} from B3LYP calculation on $P2/c$ unit cell. Mode frequencies and irreducible representations are (a) 559 cm^{-1} A_u, (b) 617 cm^{-1} A_u, (c) 573 cm^{-1} B_u, and (d) 627 cm^{-1} B_u. .

Raman active modes between 560 and 640 cm^{-1} differ in character from the 565 cm^{-1} T_{2g} modes in $Fd\bar{3}m$ $\mathrm{Fe_3O_4}$ (Fig. 11). The $8A_g$ and B_g modes between 560 and 640 cm^{-1} consist of out-of-phase breathing motions along A site Fe-O bonds, similar to the A_u and B_u IR active modes shown in Fig. 13, but are even rather than odd with respect to inversion. Ion displacements for the four B_g modes between 560 and 640 cm^{-1} are available in Ref. 52. The pattern of concentration of eigenvector amplitude for the B_g modes at 574 and 631 is the same as for the A_u and B_u IR active modes between 559 and 627 cm^{-1} (Table VI). Ion displacements are concentrated on O3+O4 ions in B2 chains, O5 ions in B3/B4 chains, O1+O2 ions in B1 chains, and O6 ions in B3/B4 chains.

The A_g mode at 584 cm^{-1} in the DFT-GGA calculation on $\mathrm{Fe_3O_4}$ in the $Fd\bar{3}m$ unit cell consists of breathing motions of A site Fe-O bonds [Fig. 11(e)]. The in-phase breathing motion induces large electronic polarizability changes with changes in phonon coordinate and hence this is the mode

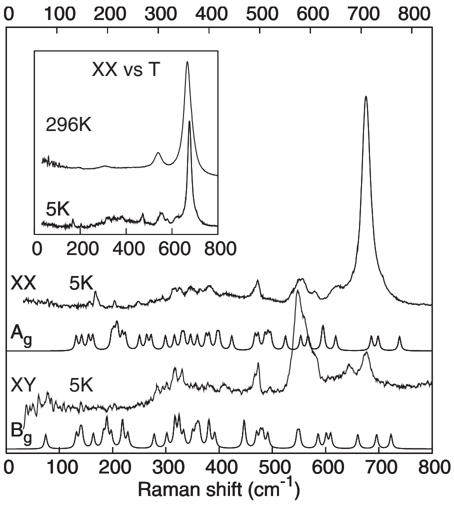

FIG. 14. Raman spectrum of Fe_3O_4 at 5 K and A_g and B_g mode densities from B3LYP calculation on Fe_3O_4 in the $P2/c$ unit cell. Experimental spectra measured in XX and XY geometries are reproduced from Ref. 42. Mode frequencies from the LO model are drawn with a scale which differs from that for experiment by 5% as explained in the text. Inset shows the variation in the Raman spectrum with temperature below and above T_V

with the greatest Raman cross section. The $8A_g$ and B_g modes in the $P2/c$ unit cell between 650 and 800 cm^{-1} also consist of breathing motions of A site Fe-O bonds. Mode frequencies and concentration of ion displacements on specific O ions are given in Table VII. Eigenvectors corresponding to the B_g mode at 693 cm^{-1} and the A_g mode at 720 cm^{-1} are shown in Fig. 15. They have a breathing character about A site Fe^{3+} sites but concentration of the modes on particular O sites results in a "half-breathing" mode.

TABLE VII. Raman active A_g and B_g phonon modes between 560 and 640 cm^{-1} and between 650 and 800 cm^{-1} from B3LYP calculation on Fe_3O_4 in the $P2/c$ unit cell. Ion sites on which phonon amplitudes are primarily concentrated and mode frequencies in cm^{-1} are given.

Freq.	Irrep.	Eigenvector
581	A_g	O2 O3
595	A_g	O1 O2
624	A_g	O5 O6
626	A_g	O2 O3 O4
574	B_g	O3 O4
578	B_g	O5
615	B_g	O1 O2
631	B_g	O6
650	A_g	O2 O5b
720	A_g	O5 O6
733	A_g	O3 O4
775	A_g	O1 O2 O6
639	B_g	O2 O5
693	B_g	O3 O4
731	B_g	O2 O5
759	B_g	O1 O2 O6

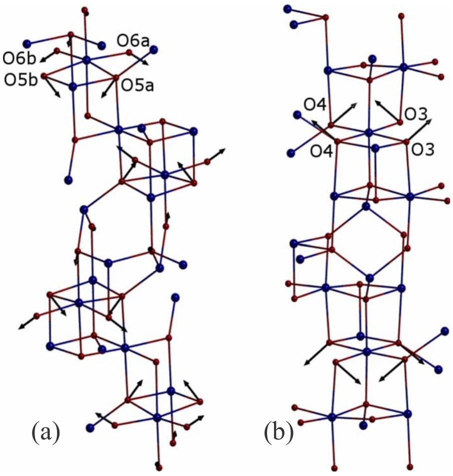

FIG. 15. (Color online) Raman active phonon eigenvectors from B3LYP calculation on Fe_3O_4 in the $P2/c$ unit cell between 650 and 800 cm^{-1}. (a) 720 cm^{-1} (A_g); (b) 693 cm^{-1} (B_g).

III. DISCUSSION

A. Crystal structure

The charge ordered state of magnetite below T_V is characterized by distortions of Fe B site octahedra,[8] disproportionation of charge,[8,9,12] and magnetic moments between B site octahedra and opening of a d-d optical band gap.[53] Octahedra surrounding B1 and B4 sites are expanded relative to B2 and B3 sites with mean Fe-O bond lengths of 2.072 Å (2.099) for the B1 site from experiment[8] (or B3LYP energy minimization), 2.069 Å (2.098) for the B4 site, 2.043 Å (2.016) for the B2 site, and 2.050 Å (2.027) for the B3 site. Similar computed mean Fe-O bond lengths were obtained in a GGA+U energy minimization calculation by Pinto and Elliott.[19] Mean bond lengths obtained were 2.111 Å (B1), 2.108 Å (B4), 2.033 Å (B2), and 2.045 Å (B3). Both energy minimization calculations predict B1 and B4 mean bond lengths to be greater than experiment by 0.03–0.04 Å and they predict B2 and B3 mean bond lengths to be shorter than experiment by 0.01–0.03 Å. As noted in Sec. II C, the pattern of Jahn-Teller distortions about Fe B sites can be understood in terms of the particular pattern of orbital order found on those sites.

B. Charge order

BVSs calculated from alternation in mean Fe-O bond length in B site octahedra have been interpreted as experimental evidence for charge order in magnetite;[8] Fe B1 and B4 sites were found to have a valence of +2.4 while B2 and B3 sites have a valence of +2.6. Differences in net electronic charges on these sites have been calculated in DFT+U, SIC-DFT, and B3LYP functional calculations in order to obtain a theoretical estimate of the degree of charge disproportionation and charge order in magnetite. Here the charge disproportionation parameters were found to be $\delta_{12}=0.18$ for B1 and B2 sites and $\delta_{34}=0.16$ for B3 and B4 sites. Jeng *et al.*[18] investigated the dependence of charge disproportionation on the Hubbard U parameter in their DFT+U calculations. They found a charge disproportionation of 0.11e and zero electronic band gap for a U value of 4.0 eV, which increased to 0.19e and a band gap of 0.63 eV when U was increased to 5.5 eV. The optimal value of U was found to be 4.5 eV, which yielded a charge disproportionation of 0.15e and band gap of 0.20 eV. These calculations were performed using the crystal structure of Wright *et al.*;[8] when the crystal structure was allowed to relax the charge disproportionation remained fixed at 0.15e and the band gap increased to 0.44 eV.[18] Using a U value of 6.21 eV,[17] Madsen and Novak[17] found a charge disproportionation of 0.24e and Leonov *et al.*[20] found a charge disproportionation of 0.24e and a band gap of 0.18 eV using a U value of 5.0 eV. Szotek *et al.*[14] found a charge disproportionation of 0.36e and a band gap of 0.35 eV for the SIC-DFT ground state in the $P2/c$ unit cell. The measures of charge disproportionation used in calculations and experiment differ considerably; estimates by experimentalists were based on crystal structure and bond valence sums while estimates by theoreticians are based on projections of charge onto Fe B sites. Charge disproportionation estimates from DFT+U calculations[17,18,20] were based on total charges within spheres of limited radii centered on Fe B sites, while the B3LYP calculations reported here used a Mulliken population analysis. Nevertheless, all estimates show that the extent of charge disproportionation is apparently much less than complete disproportionation into Fe^{2+} and Fe^{3+} ions.

DFT+U studies which reported orbital ordering,[11,15,19,20] as well as the B3LYP calculations reported here, all yield essentially the same electronic band structure and charge and orbital ordered state for Fe_3O_4 in the $P2/c$ unit cell. The eight conduction electron bands around −2 eV in the right panel of Fig. 6 are localized on B1 and B4 sites. Density of states contributions to those bands from O or other Fe A or B sites are small. The orbital order of this state, shown in Figs. 8 and 9, contains ordered t_{2g} electrons on B1 and B4 sites; the spherical density found on the B3 site (Fig. 9) is a screening charge from deeper in the valence band. These charges maintain a degree of charge neutrality over the B sites and reduce the charge disproportionation to the low observed values of ~0.1.

The $P2/c$ unit cell used here and in most recent computational work is not the full unit cell for Fe_3O_4. One study[18] has considered charge order in the full Cc space group and finds that when this structure is relaxed, charge and orbital order along B1 chains is the same as in the $P2/c$ unit cell, but an alternating occupied/unoccupied order develops on B2 and B3/B4 chains. The well known Anderson criterion[36] for minimal Coulomb repulsion in the magnetite structure requires that each cube contains two Fe^{2+} and two Fe^{3+} ions. Neither of the charge order patterns found here or in earlier studies[11,15,19,20] in the $P2/c$ or Cc unit cells[18] fulfills this criterion. Coulomb repulsion obviously becomes less important where large screening charges are generated which minimize charge disproportionation between similar sites.

The original conjecture on charge ordering in Fe_3O_4 by Verwey and Heilmann[35] conceived the charge order as localized Fe^{2+} and Fe^{3+} ions on octahedral sites. Recent experimental and computational studies discussed above have found that the degree of charge disproportionation, δ_{12} and δ_{34}, between B sites is much less than a full electronic charge. However, Verwey and Heilmann[35] *were essentially correct* in their conjecture since all conduction electrons do localize fully on octahedral B sites below T_V, although the actual charge ordering pattern is different. As far as the current authors are aware, this has not been explicitly stated in any of the recent theoretical work on Fe_3O_4.

C. Hybrid functionals and related methods

Since the charge order predicted by B3LYP is the same as that predicted by DFT+U methods, it is worth placing the former approach in context. The Kohn-Sham matrix in hybrid density functionals contains the HF exchange operator with a weighting factor. HF exchange in the HF approximation [$A=1$, $B=C=0$ in Eq. (1)] overestimates the band gaps of solids; predicted band gaps of solids are linearly dependent on any simple weighting factor attached to HF exchange in the exchange operator.[30] It is well known that the GW approximation predicts band gaps of semiconductors and insulators very well. The GW approximation is essentially a dynamically screened HF theory in which the HF exchange is screened (or weighted) by the energy and wave vector dependent inverse dielectric function. The dependence of the screening of states around the band gaps in semiconductors is only weakly energy and wave vector dependent. The extent of uniform screening of the HF exchange operator in the GW approximation by the "head" of the dielectric matrix is on the order of the reciprocal of the electronic dielectric constant, $1/\epsilon_\infty \sim 0.2$, for many oxides. Hence there are some similarities between hybrid density functionals and the GW approximation.

Magnitudes of HF exchange matrix elements in transition metal oxides are very different for transition metal 3d states and oxygen 2p states. In NiO the Ni 3d exchange energy calculated with either self-consistent HF theory or B3LYP is around −45 eV for majority spin states.[54] In contrast, the oxygen 2p exchange energy is around −27 eV and the exchange energy for the lowest conduction band is around −11 eV. Inclusion of HF exchange lowers the energies of occupied states more than unoccupied states and compact states such as d states are lowered more in energy and become more compact to a greater extent. DFT+U methods also result in greater localization of transition metal d states through the U term. If the parallel drawn between GW and hybrid density functionals is indeed valid, then in a narrow gap oxide such as Fe_3O_4, with greater screening than a typical oxide, a smaller weight for HF exchange ($A=0.15$ rather than 0.20) is likely to be needed in order to account for the degree of charge disproportionation, band gap opening, and extent of bond length distortion in the charge ordered state.

D. Phonons and vibrational spectra

The nature of the Verwey transition has been debated over many years.[1,4–15,21,36,55] While there is an abrupt change in electric conductivity at T_V, by about 2 orders of magnitude,[1] other probes such as neutron diffuse scattering indicate that there are strong fluctuations in the cubic phase well above T_V. Neutron diffuse scattering extends up to 100 K above T_V and disappears abruptly below T_V.[4,5] It has been proposed[55] that the electronic and crystal structure symmetry breaking about Fe B sites, which is observed in Fe_3O_4 below T_V,[8] is actually present above T_V. Models including existence of "molecular polarons"[5] and dynamical distortions[55] which condense at T_V have been advanced. In this scenario the Verwey transition is essentially an ordering of the lattice polarons which form about Fe B sites with an extra electron once the thermal energy of the polarons is low enough to allow them to condense. This ordering would then be accompanied by the 2 orders of magnitude drop in conductivity which occurs on cooling through T_V.[1] In the work reported here, it has been shown that the highest frequency breathing mode phonons in Fe_3O_4 below T_V are localized in layers. This localization may have an important part to play in the drop in conductivity at T_V.

If the evolution of IR and Raman spectra through T_V is examined in the context of this model, the following observations can be made: linewidths of the two main IR active modes above T_V at 350 and 600 cm^{-1} are fairly broad at 24 and 26 cm^{-1}, respectively.[42] These widths are large but are not much greater than linewidths in other spinels without charge order.[56] Increases in linewidth on cooling through T_V in this scenario must be due to charge ordering, which produces the splitting of frequencies found in the calculations reported above; the Raman spectrum at 125 K (Ref. 45) is essentially the same as the spectrum at 300 K in terms of the number of modes, but the linewidth of the E_g mode around 300 cm^{-1} is very broad ($\sim$100 cm^{-1}) just above T_V at 125 K, suggesting a degree of disorder about Fe B sites, and evolves into the broad band of modes between 200 and 500 cm^{-1} on cooling below T_V. Extra peaks in the spectrum appear abruptly between 120 and 116 K and are fully established at 100 K.

The most striking finding in the work reported here is that phonons in the highest IR band and two highest Raman bands are concentrated on specific B site chains in the low temperature phase and that there are splittings in mode frequencies by $\sim$50 cm^{-1} for the 565 cm^{-1} mode (540 cm^{-1} in experiment) and by $\sim$120 cm^{-1} for the 584 cm^{-1} mode (670 cm^{-1} in experiment). The Raman spectrum below T_V shows a line narrowing by 10 cm^{-1} (Ref. 42) and new modes appear either as distinct peaks or shoulders to strong peaks. These additional peaks may be the frequency-split peaks predicted in these calculations. Presumably one mode retains most of the Raman scattering cross section, but other frequency-split modes also have some cross section. Such a redistribution of scattering cross section may explain the observed narrowing of the band observed at 670 cm^{-1} by 10 cm^{-1} when Fe_3O_4 is cooled through T_V. Charge ordering in Fe_3O_4 has been shown to have a predominant [001] charge density modulation accompanied by a weaker $[00\frac{1}{2}]$ modulation;[8] magnetic inelastic neutron scattering from Fe_3O_4 exhibits a 7 meV gap in the spin wave spectrum midway to the Brillouin zone boundary for **q** vectors parallel to the *c* axis.[57] It is therefore not surprising to find strong modulations of ion displacements in phonon modes along the *c* axis. Further experimental and theoretical work, including computed Raman cross sections, is needed to resolve the number and polarization of additional modes which are observed below T_V around 600 cm^{-1}.

There is one unstable mode of A_g symmetry in the phonon calculation on Fe_3O_4 in the $P2/c$ unit cell. It is concentrated mainly on Fe A2 and B3 and O6 sites and displacements are mainly parallel to the *b* axis. The CRYSTAL package computes analytic derivatives of the total energy with respect to ion displacement[58,59] (i.e., forces on the ion including Pulay forces[60]) at several points in order to obtain numerical second derivatives of the total energy. These forces are evaluated using highly converged wave functions at each ion displacement and so the force constant matrix generated should be an excellent numerical approximation to the force constant matrix within the approximations of the B3LYP functional and computational conditions used. The phonon calculation in the $P2/c$ unit cell was repeated several times under different computational conditions and the unstable mode was present in each case. The instability in the $P2/c$ structure is likely to be caused either by the B3LYP functional or the $P2/c$ approximation to the full Cc unit cell found in experiment.[8,49] The Cc structure is obtained from the $P2/c$ structure by doubling the unit cell along the *a* and *b* crystallographic axes. A recent DFT+Hubbard U calculation, in which the crystal lattice was relaxed in both the $P2/c$ and Cc unit cells, found a different charge order for the Cc unit cell in sites corresponding to B3/B4 chains.[18] The latter charge order is similar to the charge order pattern found by refinement of resonant x-ray diffraction studies of Fe_3O_4 (Ref. 12); the unstable mode whose ion displacements are concentrated on Fe and O sites in the B3 chains of the $P2/c$ unit cell may be an indication that the charge order found in the $P2/c$ unit cell is not the ground state in the Cc supercell.

E. Verwey transition and charge transport

The main focus of this paper is the structure and vibrational spectra of magnetite above and below T_V. In this section we consider the implications of our results for the Verwey transition itself. The relative importance and actual nature of the changes which occur in magnetite on passing through T_V continue to be debated. A key question in this debate is whether or not a gap exists in the density of states above T_V.

Experimental evidence from photoemission and inverse photoemission has been used to argue for and against the existence of a gap above T_V. One study reported a gap of 70 meV below T_V which closed on raising the temperature above T_V[61]; in another study a gap observed below T_V was reduced by 50 meV above T_V but did not close completely.[62] A more recent soft x-ray photoemission study reported a discontinuous change in photoemission onset by 50 meV which occurs sharply at T_V.[10] The authors of that work fitted the photoemission line shape within 1 eV of the onset for photoemission to a small polaron Gaussian line shape. They also noted the absence of a metallic Fermi edge or conventional quasiparticle.[10] Similar photoemission line shapes have been observed in a cuprate at low hole doping and the absence of a quasiparticle peak and good fit by a small polaron Gaussian profile were reported recently.[63] The gap in the density of states of magnetite below T_V obtained by optical conductivity measurements has been reported to be 200 meV[42] or 140 meV.[53] A strong polaronic peak observed in the optical conductivity around 0.6 eV, when the sample is below T_V, weakens considerably above T_V.[42,53]

We now consider creation of small polaron charge carriers in the charge and orbitally ordered state predicted by our hybrid DFT calculations on the $P2/c$ structure. Creation of a small polaron hole state will occur with removal of a minority spin electron from either a B1 or B4 site while creation of a small polaron electron state will occur with addition of an electron to a B2 or B3 site. Charge transport in magnetite below T_V is expected to occur via creation of pairs of small polaron electrons and holes and drift of these heavy carriers in an electric field. Our finding that minority spin d electrons on B sites are well localized, and that this is accompanied by only a small total disproportionation of charge in agreement with experiment,[12] is obviously important to the small polaron model of charge carriers in magnetite. The Verwey transition is accompanied by a structural change from a monoclinic to a cubic structure. This change in structure may be expected to cause a significant change in conductivity as small polaron electron-hole pairs are not condensed into the charge ordered ground state found below T_V.

Hybrid DFT (this work) and LDA+U calculations predict a charge ordered state with charge and orbitally ordered minority spin d electrons and a monoclinic crystal structure. The GGA-DFT calculations reported here predict an itinerant electron state and a cubic crystal structure. A dynamical mean field theory (DMFT) calculation performed using a density of states derived from a local spin density approximation (LSDA) calculation predicts a semiconducting state for magnetite above and below T_V.[23] The small polaron electron and hole states referred above are not included in any of these calculations as none of them includes coupling of phonons to charge carriers. The hybrid DFT methods that have been used in this work predict a small polaron state for holes introduced into a cuprate at low hole density and a polaronic optical transition at midgap.[64] Work in progress on magnetite[65] shows that adding electrons or holes to magnetite in hybrid DFT calculations does indeed result in small polaron states. The strongly temperature dependent conductivity in magnetite above and below T_V is likely to be strongly associated with an activation barrier to small polaron hopping.

The GGA-DFT calculations reported here predict the crystal structure, lattice parameter, and vibrational frequencies of magnetite above T_V in good agreement with experiment.[8] However, the GGA-DFT Hamiltonian omits electron-phonon coupling which is evidently important in charge transport in magnetite and hence the itinerant electron metallic state which it predicts will not give reliable predictions of charge transport properties above T_V. A recent DMFT study of magnetite[23] used the density of states derived from an LSDA calculation on the cubic magnetite structure and found that the itinerant metallic state from LSDA was replaced by two possible charge gapped states whose gaps differed by 24 meV.[23] These were interpreted as the states observed by photoemission and inverse photoemission where the gap decreased by 50 meV on crossing T_V from below.[62] The DMFT study did not consider the change in structure at T_V and attributed the opening of the charge gap to Fe d state electron correlations. There is abundant experimental evidence that charge carriers exist as small polarons in transition metal oxides.[66] Inclusion of both electron-phonon coupling and electron correlations is evidently essential for understanding transport properties of these systems.

IV. CONCLUSION

In conclusion, the crystal and electronic structures of Fe_3O_4 in the $Fd\bar{3}m$ and $P2/c$ unit cells have been calculated using DFT-GGA and B3LYP hybrid density functional methods. Structure relaxations in the $P2/c$ unit cell using the B3LYP functional find only relatively small differences from the structure refined from x-ray and neutron scattering data.[8] Both structures are characterized by alternation in the mean Fe-O bond length in Fe B site octahedra along the crystalline c axis. A similar modulation is found in B3LYP functional calculations reported here and in similar calculations which used a DFT-GGA+U functional;[19] however, both calculations predict a larger degree of modulation than was obtained from experiment.[8] The modulation in crystal structure is accompanied by a charge disproportionation between B1/B2 and B3/B4 octahedral Fe sites. Bond valence sums computed from the experimental crystal structure imply a difference in valence of the Fe ions at these sites of 0.2, much less than the difference between their formal valences (+2/+3). Estimates of charge disproportionation based on GGA-DFT+U, SIC-DFT, or B3LYP functional calculations range from 0.20e (Ref. 18) to 0.36e (Ref. 14); the B3LYP calculation predicts a disproportionation of $\delta_{12}=0.18e$ and $\delta_{34}=0.14e$. The minority spin valence band contains an isolated group of eight bands at the valence band maximum. Electrons in these bands are strongly localized on Fe B1 and B4 sites, showing that conduction electrons are indeed localized on specific Fe octahedral sites formally as Fe^{2+} or Fe^{3+}, but with a different ordering pattern from that originally envisaged by Verwey.

Vibrational modes of Fe_3O_4 in the cubic high temperature $Fd\bar{3}m$ and monoclinic low temperature $P2/c$ unit cells have been computed using DFT-GGA and B3LYP hybrid DFT functionals, respectively. There is good agreement between IR and Raman active mode frequencies for the $Fd\bar{3}m$ phase with a 30.9 cm^{-1} mean absolute difference between experimental mode frequencies and predicted frequencies. The IR conductivity for the $P2/c$ phase was calculated using a Lorentz oscillator model and eigenmodes calculated using a B3LYP functional. When B3LYP mode frequencies are scaled down by 5% there is good agreement between peak positions in the LO model and experiment. Increases in IR linewidth from 24 to 39 and from 26 to 36 cm^{-1} are observed in experiment on cooling through T_V.[42] This may be explained by the appearance of a number of new IR active modes as the symmetry is broken on going from the $Fd\bar{3}m$ to the $P2/c$ structure.

There are major changes in the Raman spectrum on cooling through T_V. Raman active mode densities at the Γ point

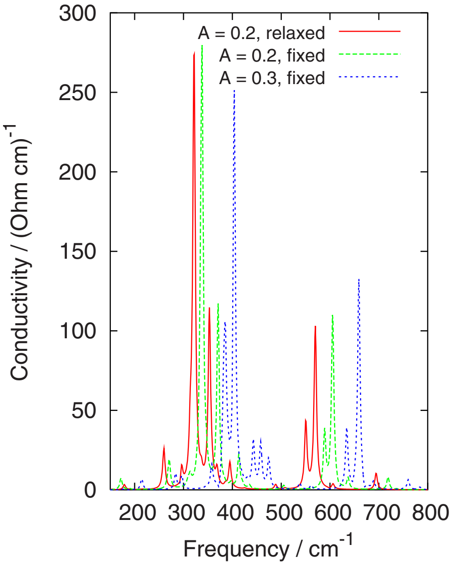

FIG. 16. (Color online) Conductivity of Fe_3O_4 parallel to the c axis computed using a B3LYP functional and the LO model in Eq. (2) with lattice constants fixed at experimental values or fully relaxed and with weights of HF exchange, $A=0.2$ or 0.3.

of appropriate symmetry are compared to polarized Raman spectra. There is good agreement in distributions of mode frequencies for both A_g and B_g modes when compared to polarized Raman spectra in experimental XX and XY geometries, except for the XY spectrum below 300 cm^{-1}. In the $Fd\bar{3}m$ structure the two most intense lines are found at 540 (T_{2g}) and at 670 cm^{-1} (A_g). In the $P2/c$ structure each of these modes is replaced by $4A_g$ and $4B_g$ Raman active modes which are split in frequency by 50 or 100 cm^{-1}. This splitting occurs because charge ordering, which accompanies the transition between the cubic $Fd\bar{3}m$ and monoclinic $P2/c$ structures, induces symmetry breaking in force constants on Fe octahedral B sites. A detailed comparison of Raman line positions and intensities from theory and experiment would provide a powerful probe of the Verwey transition.

ACKNOWLEDGMENTS

The authors are grateful to David Tanner for helpful discussions and for use of IR data on magnetite reproduced from Fig. 12 of Ref. 42. C.H.P. acknowledges discussions with Paul Attfield on x-ray and neutron scattering work in Ref. 8 and with Roberto Dovesi on choices of computational parameters. This work was supported by the Irish Higher Education Authority (IHEA) under Program No. PRTLI3-IITAC2. Computer time was provided by the Trinity Centre for High Performance Computing which is supported by the IHEA, Science Foundation Ireland, and the Irish National Development Plan. L.V.G. acknowledges support by the National Science Foundation under Grant No. DMR-08-05-073, Research Corporation Cottrell College Science under Grant No. CC 6130, Petroleum Research Fund under Grant No. 40926-GB10, and Office of Naval Research (ONR) under Grant No. N00014-06-1-0133.

APPENDIX: DETAILS OF CALCULATIONS

All electron Gaussian orbital basis sets used in this work are an Fe $20s12p6d$ basis contracted to $5s4p2d$, previously used to study hematite[67] and a $14s6p$ basis contracted to $4s3p$, previously used to study NiO.[68] Integration over the Brillouin zone was done using $4\times4\times4$ or $6\times6\times6$ (phonon calculations only) Monkhorst-Pack nets[69] for the $P2/c$ unit cell and a $6\times6\times6$ net for the $Fd\bar{3}m$ unit cell. Lattice sum tolerances of 7 7 7 7 14 and the densest standard grid for integration in the DFT part of the Hamiltonian in the CRYSTAL package were used. Figure 2 was produced using the XCRYSDEN visualization package[70] and phonon eigenvectors were drawn using the MOLDRAW package.[71]

Vibrational modes of Fe_3O_4 at the Γ point of the Brillouin zone were calculated using the CRYSTAL package[48,58] and the B3LYP hybrid functional.[72,73] Vibrational frequencies of the magnetic insulator, andradite $Ca_3Fe_2Si_3O_{12}$, calculated using the CRYSTAL package, have a mean absolute error less than 10 cm^{-1} (Ref. 74) when compared to experiment. A study of the relative accuracies of HF, B3LYP, local density approximation (LDA) and Perdew-Burke-Enzerhof (PBE) functionals for calculating vibrational mode frequencies of α quartz at the Γ point found mean absolute errors of 44, 5.8, 17.5, and 21.0 cm^{-1} and maximum absolute errors of 85.2, 22.1, 42.6, and 40.1 cm^{-1}, respectively.[58] The mean absolute error in the phonon calculation on $Fd\bar{3}m$ Fe_3O_4 presented here was 30.9 cm^{-1} and the maximum absolute error was 86 cm^{-1} for the A_g mode. This breathing mode is predicted to lie at a very similar frequency by another DFT-GGA calculation,[22] whereas frequencies predicted by B3LYP for equivalent modes in the $P2/c$ unit cell are much closer to the experimental value of 670 cm^{-1}. These larger errors likely reflect the more complex electronic structure of a narrow gap or metallic oxide compared with quartz, which is a wide gap insulator. Magnitudes of frequencies of modes which correspond to lattice translations were around 1 cm^{-1}.

The effect of lattice constant and weight of HF exchange in the functional on vibrational frequencies is illustrated in Fig. 16. There is a small downward shift in peaks in the conductivity spectrum when lattice constants are relaxed and there are only minor changes in the shape of the spectrum. Increasing the weight of HF exchange in the functional shifts frequencies upward by about 10%.

[1] E. J. W. Verwey, Nature (London) **144**, 327 (1939).

[2] E. J. W. Verwey and P. W. Haayman, Physica **8**, 979 (1941).

[3] P. W. Anderson, Phys. Rev. **115**, 2 (1959).

[4] S. M. Shapiro, M. Iizumi, and G. Shirane, Phys. Rev. B **14**, 200 (1976).

[5] Y. Yamada, N. Wakabayashi, and R. M. Nicklow, Phys. Rev. B **21**, 4642 (1980).

[6] J. M. Zuo, J. C. H. Spence, and W. Petuskey, Phys. Rev. B **42**, 8451 (1990).

[7] P. Novák, H. Stěpánková, J. Englich, J. Kohout, and V. A. M. Brabers, Phys. Rev. B **61**, 1256 (2000).

[8] J. P. Wright, J. P. Attfield, and P. G. Radaelli, Phys. Rev. B **66**, 214422 (2002).

[9] R. J. Goff, J. P. Wright, J. P. Attfield, and P. G. Radaelli, J. Phys.: Condens. Matter **17**, 7633 (2005).

[10] D. Schrupp, M. Sing, M. Tsunekawa, H. Fujiwara, S. Kasai, A. Sekiyama, S. Suga, T. Muro, V. A. M. Brabers, and R. Claessen, Europhys. Lett. **70**, 789 (2005).

[11] D. J. Huang *et al.*, Phys. Rev. Lett. **96**, 096401 (2006).

[12] E. Nazarenko, J. E. Lorenzo, Y. Joly, J. L. Hodeau, D. Mannix, and C. Marin, Phys. Rev. Lett. **97**, 056403 (2006).

[13] G. K. Rozenberg, M. P. Pasternak, W. M. Xu, Y. Amiel, M. Hanfland, M. Amboage, R. D. Taylor, and R. Jeanloz, Phys. Rev. Lett. **96**, 045705 (2006).

[14] Z. Szotek, W. M. Temmerman, A. Svane, L. Petit, G. M. Stocks, and H. Winter, Phys. Rev. B **68**, 054415 (2003).

[15] H.-T. Jeng, G. Y. Guo, and D. J. Huang, Phys. Rev. Lett. **93**, 156403 (2004).

[16] I. Leonov, A. N. Yaresko, V. N. Antonov, M. A. Korotin, and V. I. Anisimov, Phys. Rev. Lett. **93**, 146404 (2004).

[17] G. K. H. Madsen and P. Novak, Europhys. Lett. **69**, 777 (2005).

[18] H.-T. Jeng, G. Y. Guo, and D. J. Huang, Phys. Rev. B **74**, 195115 (2006).

[19] H. P. Pinto and S. D. Elliott, J. Phys.: Condens. Matter **18**, 10427 (2006).

[20] I. Leonov, A. N. Yaresko, V. N. Antonov, and V. I. Anisimov, Phys. Rev. B **74**, 165117 (2006).

[21] P. Piekarz, K. Parlinski, and A. M. Oles, Phys. Rev. Lett. **97**, 156402 (2006).

[22] P. Piekarz, K. Parlinski, and A. M. Oles, Phys. Rev. B **76**, 165124 (2007).

[23] L. Craco, M. S. Laad, and E. Müller-Hartmann, Phys. Rev. B **74**, 064425 (2006).

[24] M. Iizumi and G. Shirane, Solid State Commun. **17**, 433 (1975).

[25] J. Yoshida and S. Iida, J. Phys. Soc. Jpn. **47**, 1627 (1979).

[26] P. A. M. Dirac, Proc. Cambridge Philos. Soc. **26**, 376 (1930).

[27] A. D. Becke, Phys. Rev. A **38**, 3098 (1988).

[28] C. Lee, W. Yang, and R. G. Parr, Phys. Rev. B **37**, 785 (1988).

[29] S. H. Vosko, L. Wilk, and M. Nusair, Can. J. Phys. **58**, 1200 (1980).

[30] F. Cora, M. Alfredsson, G. Mallia, D. S.Middlemiss, W. C. Mackrodt, R. Dovesi, and R. Orlando, Struct. Bonding (Berlin) **113**, 171 (2004).

[31] L. Hedin, Phys. Rev. **139**, A796 (1965).

[32] F. Aryasetiawan and O. Gunnarsson, Rep. Prog. Phys. **61**, 237 (1998).

[33] J. P. Wright, J. P. Attfield, and P. G. Radaelli, Phys. Rev. Lett. **87**, 266401 (2001).

[34] A. J. M. Kuipers and V. A. M. Brabers, Phys. Rev. B **20**, 594 (1979).

[35] E. J. W. Verwey and E. L. Heilmann, J. Chem. Phys. **15**, 174 (1947).

[36] P. W. Anderson, Phys. Rev. **102**, 1008 (1956).

[37] G. Subias, J. Garcia, J. Blasco, M. Grazia Proietti, H. Renevier, and M. Concepcion Sanchez, Phys. Rev. Lett. **93**, 156408 (2004).

[38] R. D. Waldron, Phys. Rev. **99**, 1727 (1955).

[39] W. B. White and B. A. DeAngelis, Spectrochim. Acta, Part A **23**, 985 (1967).

[40] J. L. Verble, Phys. Rev. B **9**, 5236 (1974).

[41] L. Degiorgi, I. Blatter-Mörke, and P. Wachter, Phys. Rev. B **35**, 5421 (1987).

[42] L. V. Gasparov, D. B. Tanner, D. B. Romero, H. Berger, G. Margaritondo, and L. Forró, Phys. Rev. B **62**, 7939 (2000).

[43] C. M. Julien and M. Massot, Mater. Sci. Eng., B **97**, 217 (2003).

[44] O. N. Shebanova and P. Lazor, J. Solid State Chem. **174**, 424 (2003).

[45] L. V. Gasparov, D. Arenas, K.-Y. Choi, G. G'untherodt, H. Berger, L. Forro, G. Margaritondo, V. V. Struzhkin, and R. Hemley, J. Appl. Phys. **97**, 10A922 (2005).

[46] B. Handke, A. Kozlowski, K. Parlinski, J. Pzrzewoznik, T. Slezak, A. I. Chumakov, L. Niesen, Z. Kakol, and J. Korecki, Phys. Rev. B **71**, 144301 (2005).

[47] J. P. Perdew and Y. Wang, Phys. Rev. B **45**, 13244 (1992).

[48] R. Dovesi *et al.*, *Crystal06 User's Manual* (University of Torino, Torino, 2007).

[49] M. Iizumi, T. F. Koetzle, G. Shirane, S. Chikazumi, M. Matsui, and S. Todo Acta Crystallogr., Sect. B: Struct. Crystallogr. Cryst. Chem. **38**, 2121 (1982).

[50] E. J. W. Verwey, P. W. Haayman, and F. C. Romeijn, J. Chem. Phys. **15**, 181 (1947).

[51] P. Graves, C. Johnston, and J. Campaniello, Mater. Res. Bull. **23**, 1651 (1988).

[52] See EPAPS document No. E-PRBMDO-79-073916 for phonon eigenvectors with (i) largest optical activity in the band between 300 and 400 wave numbers and (ii) Raman activity and B_g symmetry in the band between 560 and 640 wave numbers. For more information on EPAPS, see http://www.aip.org/pubservs/epaps.html.

[53] S. K. Park, T. Ishikawa, and Y. Tokura, Phys. Rev. B **58**, 3717 (1998).

[54] C. H. Patterson, Int. J. Quantum Chem. **106**, 3383 (2006).

[55] G. Subías, J. García, and J. Blasco, Phys. Rev. B **71**, 155103 (2005).

[56] A. M. Hofmeister, Am. Mineral. **86**, 1188 (2001).

[57] R. J. McQueeney, M. Yethiraj, W. Montfrooij, J. S. Gardner, P. Metcalf, and J. M. Honig, Phys. Rev. B **73**, 174409 (2006).

[58] F. Pascale, C. Zicovich-Wilson, F. Lopez, B. Civalleri, R. Orlando, and R. Dovesi, J. Comput. Chem. **25**, 888 (2004).

[59] C. Zicovich-Wilson, F. Pascale, C. Roetti, V. Saunders, R. Orlando, and R. Dovesi, J. Comput. Chem. **25**, 1873 (2004).

[60] P. Pulay, Mol. Phys. **17**, 197 (1969).

[61] A. Chainani, T. Yokoya, T. Morimoto, T. Takahashi, and S. Todo, Phys. Rev. B **51**, 017976 (1995).

[62] J. H. Park, L. H. Tjeng, J. W. Allen, P. Metcalf, and C. T. Chen, Phys. Rev. B **55**, 12813 (1997).

[63] K. M. Shen, F. Ronning, W. Meevasana, D. H. Lu, N. J. C. Ingle, F. Baumberger, W. S. Lee, L. L. Miller, Y. Kohsaka, M. Azuma, M. Takano, H. Takagi, and Z. X. Shen, Phys. Rev. B **75**, 075115 (2007).

[64] C. H. Patterson, Phys. Rev. B **77**, 094523 (2008).

[65] A. Chakrabarty and C. H. Patterson (unpublished).

[66] A. M. Stoneham, J. Gavartin, A. L. Schluger, A. V. Kimmel, D. M. Ramo, H. M. Ronnow, G. Aeppli, and C. Renner, J. Phys.: Condens. Matter **19**, 255208 (2007).

[67] M. Catti, G. Valerio, and R. Dovesi, Phys. Rev. B **51**, 7441 (1995).

[68] M. D. Towler, N. L. Allan, N. M. Harrison, V. R. Saunders, W. C. Mackrodt, and E. Aprà, Phys. Rev. B **50**, 5041 (1994).

[69] H. Monkhorst and J. D. Pack, Phys. Rev. B **13**, 5188 (1976).

[70] A. Kokalj, Comput. Mater. Sci. **28**, 155 (2003).

[71] P. Ugliengo, D. Viterbo, and G. Borzani, J. Appl. Crystallogr. **21**, 75 (1988).

[72] A. D. Becke, J. Chem. Phys. **98**, 5648 (1993).

[73] P. J. Stephens, F. J. Devlin, C. F. Chabalowski, and M. J. Frisch, J. Phys. Chem. **98**, 11623 (1994).

[74] F. Pascale, M. Catti, A. Damin, R. Orlando, V. Saunders, and R. Dovesi, J. Phys. Chem. B **109**, 18522 (2005).